



# Carbon-centric dynamics of Earth's marine phytoplankton

Adam C. Stoer<sup>a,1</sup> and Katja Fennel<sup>a</sup>

Edited by David Karl, University of Hawaii at Manoa, Honolulu, HI; received April 9, 2024; accepted August 19, 2024

Marine phytoplankton are fundamental to Earth's ecology and biogeochemistry. Our understanding of the large-scale dynamics of phytoplankton biomass has greatly benefited from, and is largely based on, satellite ocean color observations from which chlorophyll-a (Chla), a commonly used proxy for carbon biomass, can be estimated. However, ocean color satellites only measure a small portion of the surface ocean, meaning that subsurface phytoplankton biomass is not directly monitored. Chla is also an imperfect proxy for carbon biomass because cellular physiology drives large variations in their ratio. The global network of Biogeochemical (BGC)-Argo floats now makes it possible to complement satellite observations by addressing both these issues at once. In our study, we use ~100,000 water-column profiles from BGC-Argo to describe Earth's phytoplankton carbon biomass and its spatiotemporal variability. We estimate the global stock of open ocean phytoplankton biomass at ~314 Tg C, half of which is present at depths not accessible through satellite detection. We also compare the seasonal cycles of carbon biomass stocks and surface Chla visible from space and find that surface Chla does not accurately identify the timing of the peak annual biomass in two-thirds of the ocean. Our study is a demonstration of global-scale, depth-resolved monitoring of Earth's phytoplankton, which will be crucial for understanding future climate-related changes and the effects of geoengineering interventions if implemented.

ocean color | particle backscatter | fluorescence | phenology | bloom

Assessing global phytoplankton stocks is an important effort in biology. Modeling suggests that phytoplankton are responsible for about half of the net primary productivity on Earth, rivaling that of the terrestrial biosphere (1). The sinking of photosynthetically produced organic matter into the deep ocean keeps atmospheric CO<sub>2</sub> concentrations ~200 ppm below an otherwise phytoplankton-free ocean (2).

Our understanding of the meso- to global-scale distributions of phytoplankton biomass is largely based on satellite observations of chlorophyll-a (Chla), which is commonly used as a proxy for phytoplankton biomass. These space-based observations of Chla have enabled fundamental studies about how the standing stock of phytoplankton varies on a range of spatiotemporal scales (3–9). However, there are two well-recognized limitations when using satellite-based Chla. For one, satellite measurements are restricted to a surface layer called the first optical depth (10), meaning that the subsurface distributions of phytoplankton are not directly monitored. Second, Chla is not an ideal measure of phytoplankton biomass. Rather, the most ecologically and biogeochemically relevant metric for determining phytoplankton biomass is the mass of organic carbon specific to phytoplankton ( $C_{\text{phy}}$ ) (11, 12). Intracellular Chla can vary independently of  $C_{\text{phy}}$  because it is greatly influenced by a cell's physiological response to its growing conditions (e.g., temperature, nutrients, and light; 13). The decline in light with depth, for example, drives phytoplankton to up-regulate Chla via photoacclimation. Photoacclimation explains why the subsurface maximum in Chla does not share a similar subsurface maximum in  $C_{\text{phy}}$  in large parts of the ocean (11, 14–17).

Advances in phytoplankton detection have helped tackle these limitations. In the seminal paper by Behrenfeld et al. (18), satellite-based estimates of  $C_{\text{phy}}$  were determined from particle backscattering ( $b_{\text{bp}}$ ), a bio-optical property known to correlate with  $C_{\text{phy}}$  (19, 20). Systematic subsurface monitoring of phytoplankton dynamics has been enabled by Biogeochemical-Argo (BGC-Argo) floats, a type of underwater profiling robot, that enables estimates of  $C_{\text{phy}}$  (from  $b_{\text{bp}}$ ) and Chla (from fluorescence) throughout the euphotic zone and below. Various regional studies have utilized these measurements to describe water-column stocks of  $C_{\text{phy}}$  and Chla (21–26). Occasionally these studies highlight how the physiological variability in the Chla: $C_{\text{phy}}$  ratio can greatly complicate the interpretation of spatiotemporal trends in phytoplankton biomass when Chla is used as a proxy (22, 26). For example, Vives et al. (26) showed how the onset of the spring bloom in the Southern Ocean (below 50°S) occurs several weeks after Chla begins to increase; a discrepancy that has consequences for bloom studies relying on Chla as a proxy for  $C_{\text{phy}}$ .

## Significance

The advent of satellite observations of chlorophyll-a (Chla) has revolutionized our understanding of Earth's distribution of phytoplankton. However, it is well recognized that satellites cannot detect phytoplankton below the ocean's surface and that Chla is an imperfect measure of biomass. The maturation of autonomous robots at sea now allows for global, depth-resolved estimates of phytoplankton biomass based on optical proxy observations. From these optical measurements, we estimate the stock of phytoplankton and evaluate their spatiotemporal dynamics. The seasonal cycles of estimated phytoplankton stocks and Chla visible from space show large discrepancies in most of the ocean. Our study demonstrates that profiling robots enable more reliable monitoring of Earth's phytoplankton, which is urgently needed to understand the impact of climate change.

Author affiliations: <sup>a</sup>Department of Oceanography, Dalhousie University, Halifax, NS B3H4R2, Canada

Author contributions: A.C.S. and K.F. designed the research; A.C.S. conducted the analysis; K.F. edited the paper; K.F. reviewed the paper; K.F. supervised the analysis; and A.C.S. wrote the paper.

The authors declare no competing interest.

This article is a PNAS Direct Submission.

Copyright © 2024 the Author(s). Published by PNAS. This article is distributed under Creative Commons Attribution-NonCommercial-NoDerivatives License 4.0 (CC BY-NC-ND).

<sup>1</sup>To whom correspondence may be addressed. Email: adam.stoer@dal.ca.

This article contains supporting information online at <https://www.pnas.org/lookup/suppl/doi:10.1073/pnas.2405354121/-/DCSupplemental>.

Published October 28, 2024.

The maturation of the BGC-Argo program has produced a substantial database of depth-resolved  $b_{bp}$  and Chla fluorescence ( $F_{Chla}$ ) measurements (27), allowing for depth-resolved phytoplankton biomass dynamics to be estimated on the global scale. In this study, we aim to: 1) quantify Earth's stock of phytoplankton  $C_{phy}$  and Chla, 2) identify their spatiotemporal dynamics, and 3) test how well surface Chla serves as a proxy for depth-integrated  $C_{phy}$  ( $\Sigma C_{phy}$ ).

After quality control, we obtained 99,341 bio-optical profiles from 903 BGC-Argo floats deployed in the last decade (Fig. 1; details in the *Methods* and *SI Appendix*, Fig. S1). The main analysis is based on binning these profiles for every  $10^\circ$  latitudinal band for each of the three main ocean basins (i.e., the Atlantic, Pacific, and Indian Oceans) excluding areas where the seabed is shallower than 500 m. In each of these regions, we developed a weekly climatology of Chla and  $C_{phy}$ . Profiles of  $F_{Chla}$  were adjusted using an empirical-relationship between Chla and the diffuse attenuation coefficient ( $K_d$ ) (28). This adjustment is based on the annual mean of  $K_d$  within the 1% light level in each region (*SI Appendix*, Fig. S2).  $C_{phy}$  was estimated using a linear model based on direct measurements of  $C_{phy}$  and  $b_{bp}$  at 470 nm [*Methods*; (20)]. Most floats measure  $b_{bp}$  at 700 nm, so we converted  $b_{bp}$  to 470 nm by assuming a spectral slope of 0.73 (29). To isolate the phytoplankton-specific  $b_{bp}$  signal and ensure  $C_{phy}$  always asymptotes to  $0 \text{ mg m}^{-3}$  with depth, we applied a process that effectively subtracts deep values of  $b_{bp}$  as an in situ "blank" (*Methods* and *SI Appendix*, Fig. S3). This correction assumes that  $b_{bp}$  from nonalgal particles (NAP) is essentially constant within the euphotic zone and is reasonably consistent with picophytoplankton  $C_{phy}$  estimated from cell abundance (*SI Appendix*, *Comparison with Abundance-based Estimates* and Fig. S4). Weekly averages of depth-resolved  $C_{phy}$  and Chla were calculated for each region. From these climatologies, vertically integrated (in  $\text{mg m}^{-2}$ ) and zonally integrated stocks (in Tg) were determined. Surface Chla was calculated as the averaged mixed-layer concentration. Globally integrated stocks of  $C_{phy}$  (Tg) and Chla (Tg) are obtained as the sum of all regional stocks, while globally averaged seasonal cycles are weighted by the area of each  $10^\circ$  latitudinal region. To compare  $\Sigma C_{phy}$  or surface Chla, various bloom metrics are determined (e.g., the timing of the peak), where  $\Sigma C_{phy}$  is used as the standard metric for evaluating surface Chla as its proxy.

## Results and Discussion

**Global and Regional Stocks.** We arrive at a global standing stock of  $\sim 314 \text{ Tg } C_{phy}$  and  $\sim 11.4 \text{ Tg Chla}$  (Fig. 2). The mean absolute percentage error (MAPE) multiplied by these stocks, leaves a range

in uncertainty of 213 to 414 Tg  $C_{phy}$  and 7.8 to 15.0 Tg Chla (*Methods*). The average area-normalized stocks of open ocean  $\Sigma C_{phy}$  and  $\Sigma Chla$  are  $965 (655 \text{ to } 1,273) \text{ mg m}^{-2}$  and  $35.2 (23.9 \text{ to } 46.3) \text{ mg m}^{-2}$ , respectively. The majority of the  $C_{phy}$  and Chla stocks are both present in the southern hemisphere (67% and 60%, respectively). Around 43% of  $C_{phy}$  and 35% of Chla stock is located south of  $30^\circ\text{S}$ , which includes the Southern Ocean and its subtropical boundaries: a region that represents  $\sim 32\%$  of the open ocean's surface area (Fig. 2A). As for the major ocean basins, the relative distribution of  $C_{phy}$  and Chla stocks corresponds well with their surface area. The Pacific Ocean holds  $\sim 49\%$  of the global stocks, while the Indian and Atlantic Oceans hold  $\sim 25\%$  and  $26\%$ , respectively. If we assume that  $\sim 9\%$  of the phytoplankton are in coastal areas (based on surface area alone), the global stocks are approximately  $343 \text{ Tg } C_{phy}$  and  $12.5 \text{ Tg Chla}$ , respectively.

Our estimates of  $C_{phy}$  and Chla likely involve biases due to the conversion factors we assumed constant. Our global estimates are sensitive to these assumptions, although they are robust to an alternative spatial grouping based on BGC provinces (*SI Appendix*, *Alternative Calculations of Global Stocks*). Variability in the relationship between  $C_{phy}$  and  $b_{bp}$  is the main source of uncertainty in  $C_{phy}$ , and is driven by community composition, physiology, and the concentration of NAP relative to  $C_{phy}$  (30–35). For Chla, similar uncertainties introduced by the influence of colored dissolved organic matter, NAP, and pigment composition and packaging (36) affect the adjustment made to  $F_{Chla}$  when relying on a single global relationship.

Our estimate of global phytoplankton biomass is near the lower end of previous estimates, which range from 250 and 2,400 Tg (37, 38). Unlike previous approaches, our estimate is based on depth-resolved, carbon-centric measurements from the entire euphotic zone. Previous estimates were based on either satellite-observed ocean color or cell abundance from measurements taken from water samples. Satellite-based estimates of global phytoplankton biomass rely on assumptions about the vertical structure of Chla and/or  $C_{phy}$ . For example, Antoine et al. (39) put global  $C_{phy}$  at 860 Tg assuming a global  $C_{phy}:\text{Chla}$  ratio of  $100 \text{ g } C_{phy} \text{ g Chla}^{-1}$ , which is more than double our estimate even though their global Chla stock of 8.6 Tg is about two thirds of ours (12.5 Tg). Falkowski and Raven (37) estimated global  $C_{phy}$  between 250 to 650 Tg (assuming a  $\text{Chla}:C_{phy}$  ratio between 40 and  $100 \text{ g Chla}^{-1} \text{ g } C_{phy}^{-1}$ ). Behrenfeld and Falkowski (40) made similar estimations of 300 to 750 Tg. The abundance-based estimates rely on relatively sparse, in situ observations and must make assumptions about cellular carbon concentrations. Abundance-based

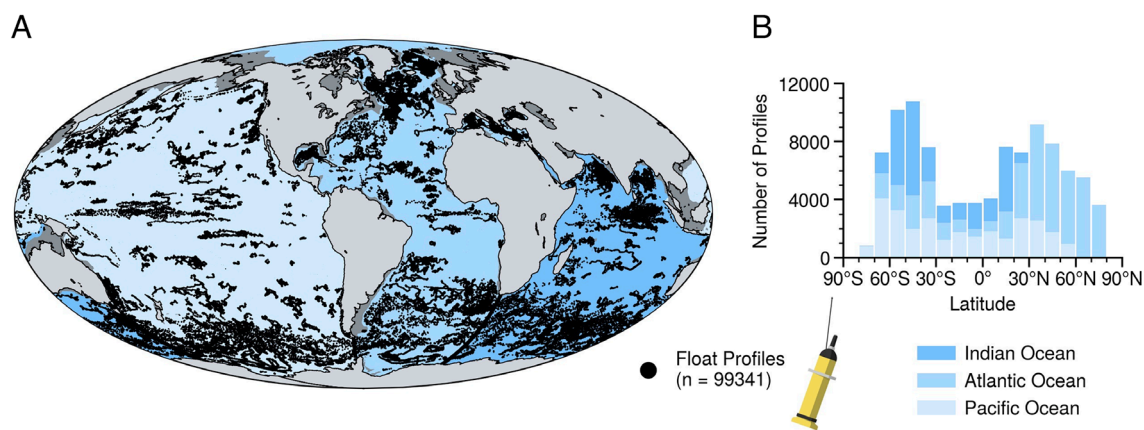


**Fig. 1.** (A) Global map of 99,341 quality-controlled, bio-optical profiles from BGC-Argo floats measuring phytoplankton Chla and  $C_{phy}$  (black points); and (B) the number of profiles obtained in every  $10^\circ$  latitudinal band for the Pacific, Atlantic, and Indian Ocean basins (colored regions). These profiles are used to calculate climatologies (e.g., surface Chla or  $\Sigma C_{phy}$ ).

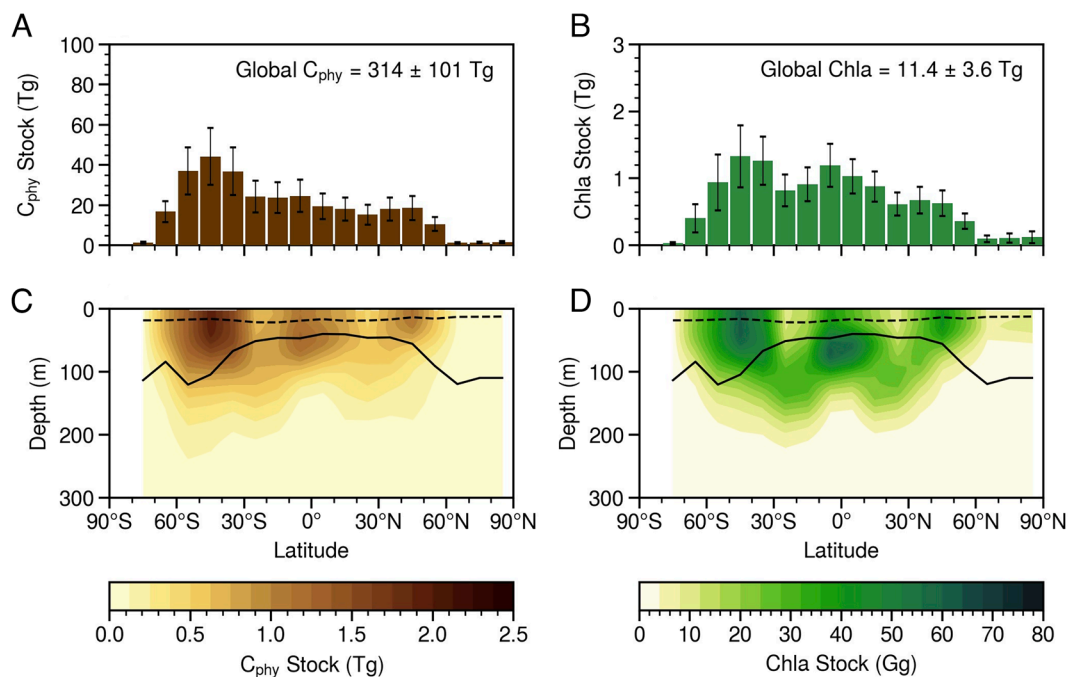


**Fig. 2.** (A and B) Latitudinal distributions of Chla and  $C_{\text{phy}}$  stock; and (C and D) vertical distributions of Chla and  $C_{\text{phy}}$  stocks per 5 m depth. The average mixed layer depth (solid black line) and first optical depth (dashed black line), weighted by the area of each ocean basin in each latitudinal band, are shown in panels C and D. Note that stocks are integrated from 0 to 500 m, although stocks below 300 m depth are either extremely low or equal to zero (main text). Coastal areas shallower 500 m are excluded from the calculation.

estimates from Buitenhuis et al. (38) put global  $C_{\text{phy}}$  between 500 and 2,400 Tg. Relying on previous estimates, a global census for all oceanic life on Earth (41) provides a best estimate of  $\sim 600$  Tg  $C_{\text{phy}}$ .

The latitudinal distribution of open ocean  $\Sigma C_{\text{phy}}$  shows a qualitatively different pattern compared to that of  $\Sigma \text{Chla}$  and Chla at the surface (Fig. 2). We do not observe any substantial differences in  $\Sigma C_{\text{phy}}$  between the subtropical gyres and the equatorial upwelling zones, in contrast to  $\Sigma \text{Chla}$  or surface Chla, which both show moderate increases at the equator (*SI Appendix, Fig. S5*). However, this difference is likely driven in part by biases in the conversion factors, which result in overestimates of  $C_{\text{phy}}$  in subtropical gyres and underestimates of  $C_{\text{phy}}$  in the Southern Ocean (33).

To understand how much phytoplankton are in the subsurface ocean and “out-of-view” of satellites, Chla and  $C_{\text{phy}}$  were vertically partitioned using the surface mixed layer depth and the first optical depth of photosynthetically active radiation (PAR) (*Methods*). Assuming a well-mixed surface, approximately half of the global  $C_{\text{phy}}$  and Chla stocks (47% and 54%, respectively) are in the surface mixed-layer and half below. An even greater portion is below the first optical depth of PAR, equal to 85% of  $C_{\text{phy}}$  and 88% of Chla, respectively. The larger portion of Chla present in the subsurface ocean, relative to  $C_{\text{phy}}$ , is owed to the photoacclimation response to declining light with depth. With either depth horizon, large portions of Earth’s phytoplankton are not directly accessible through satellite ocean color. The climatological depth of maximum Chla is also offset by more than 10 m from the depth of maximum  $C_{\text{phy}}$  in  $\sim 84\%$  of the open ocean (by surface area). Below 300 m, extremely small portions of global  $C_{\text{phy}}$  (0.4%) and Chla (0.9%) stock are present, which is consistent with expectations (30).

**Carbon and Chla Phenology.** Phytoplankton blooms, commonly used for assessing biomass phenology in ecology, are defined as periods of high phytoplankton biomass (42). Using both  $\Sigma C_{\text{phy}}$

and surface Chla, we calculated various bloom metrics along a latitudinal gradient to test how well surface Chla can be used as a proxy for  $\Sigma C_{\text{phy}}$  (Fig. 3). Metrics are described quantitatively based on the data points presented in (Fig. 3). Qualitative descriptions are based on patterns shown by generalized additive models fit to the latitudinal data.

The first metric of interest is the timing of the bloom peak and is defined as the week when  $\Sigma C_{\text{phy}}$  reaches its annual maximum. For the global ocean, we found that the average timing of the bloom peak, weighted by surface area, is  $\sim 7$  wk after surface Chla has reached its annual maximum (Fig. 3C). In the tropics ( $<30^\circ$  latitude), this difference increases to  $\sim 12$  wk on average. In about 63% of the ocean, the timing of the peak phytoplankton bloom differs by more than 4 wk to when surface Chla reaches its annual peak. The area where this discrepancy occurs, mainly equatorial and temperate latitudes, contains about half of global phytoplankton biomass (52%). The presence of other components (e.g., slow sinking detrital matter, heterotrophic bacteria) could influence these results despite our correction for NAP. Assuming such uncertainties are negligible, this result suggests that bloom peaks are misidentified by surface Chla for half of Earth’s phytoplankton. In polar oceans ( $>50^\circ$  latitude), surface Chla and  $\Sigma C_{\text{phy}}$  peaks tend to be in better synchrony (*SI Appendix, Fig. S6*).

Other aspects of the seasonal cycle in phytoplankton substantially differ from that of surface Chla as well. The blooming period, defined as the number of weeks where the rate of change in  $\Sigma C_{\text{phy}}$  is greater than  $0 \text{ d}^{-1}$  (42), ranges from approximately 19 to 26 wk and shows no clear pattern with latitude (Fig. 3D). If surface Chla is used in place of  $\Sigma C_{\text{phy}}$  to determine this metric, the latitudinal pattern in the blooming period is substantially different. On average, the blooming period based on surface Chla appears  $\sim 3$  wk longer and ranges from 22 to 31 wk. The blooming period based on surface Chla is even higher at latitudes around the subtropical gyres. For example, blooming appears to last  $\sim 12$  wk longer based on surface Chla than  $\Sigma C_{\text{phy}}$  in the region 20 to  $30^\circ \text{N}$ . In the Southern Ocean (south of  $50^\circ \text{S}$ ), blooming periods from  $\Sigma C_{\text{phy}}$  become

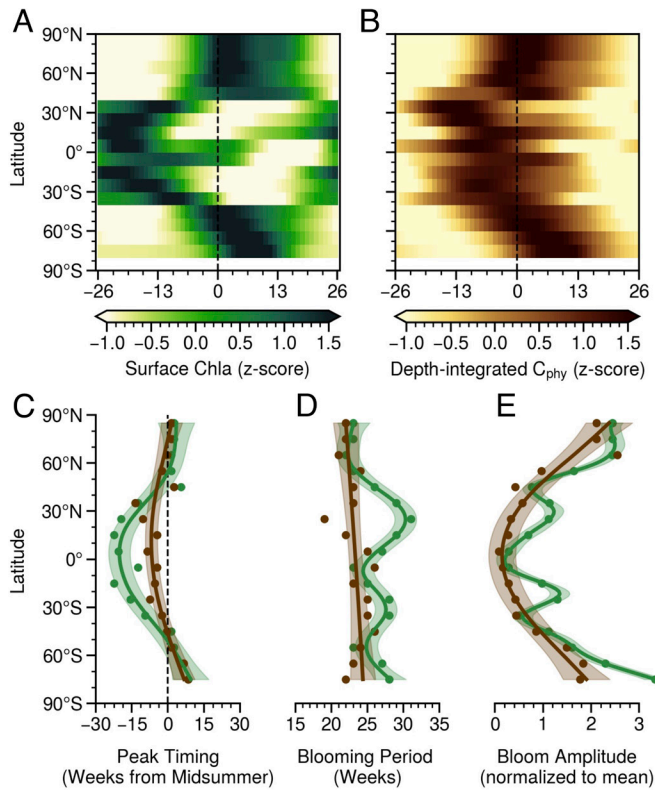


**Fig. 3.** (A and B) Seasonal cycles in phytoplankton  $\Sigma C_{\text{phy}}$  and surface Chla (as z-scores) from BGC-Argo floats. (C–E) Phenological metrics derived from the seasonal  $\Sigma C_{\text{phy}}$  and surface Chla: (C) the timing of the peak  $\Sigma C_{\text{phy}}$  and surface Chla, defined as the week from the summer solstice (midsummer); (D) the blooming period, defined as the number of weeks with a rate of change  $>0 \text{ d}^{-1}$ ; and (E) bloom amplitude, defined as the annual range normalized to the mean.

increasingly shorter with higher latitudes, which is opposite to what surface Chla suggests. This result agrees with Vives et al. (22); cf, their Fig. 2, who showed that Chla increases before phytoplankton  $C_{\text{phy}}$ , but has similar annual peaks in the Southern Ocean (south of  $50^{\circ}\text{S}$ ). This trend also is apparent in the Northern Hemisphere in regions north of  $50^{\circ}\text{N}$  (Fig. 3D).

The bloom amplitude, or the range in  $\Sigma C_{\text{phy}}$  normalized to its annual average, describes the seasonal variability in phytoplankton at each latitude (43). The bloom amplitude in  $\Sigma C_{\text{phy}}$  follows a parabolic pattern with amplitudes increasing toward the poles. The same metric calculated with surface Chla results in regional maxima around the subtropical oligotrophic gyres and polar oceans (Fig. 3E) that are not seen in its  $\Sigma C_{\text{phy}}$  counterpart. On average, the bloom amplitude based on surface Chla is twice as large as the one based on  $\Sigma C_{\text{phy}}$ , suggesting that blooms are far less pronounced than surface Chla suggests.

Other phenological metrics show differences in the cycles of surface Chla and  $\Sigma C_{\text{phy}}$  too (SI Appendix, Fig. S7). These discrepancies are well exemplified by the fact that the Pearson correlation coefficient between surface Chla and  $\Sigma C_{\text{phy}}$  is less than 0.5 in  $\sim 58\%$  of the ocean and less than 0 for  $\sim 35\%$  of the ocean (by surface area; SI Appendix, Fig. S6). Some of these discrepancies could partly be due to factors not directly influenced by phytoplankton biomass or Chla. Overall, these metrics indicate that phytoplankton blooms are shorter, less intense, and peak later in the year compared to what Chla concentrations at the surface suggest.

We also compared our float-based climatology of surface Chla with that detected by satellites over a similar period. Although individual profiles were not matched up with satellite-based values, the seasonal cycle in surface Chla correlates well with that of

satellite estimates of Chla (SI Appendix, Fig. S6). This is also supported by the fact that the bloom metrics calculated from satellite surface Chla share the same trends as those calculated from surface Chla from floats (SI Appendix, Fig. S8). This comparison implies that the climatological patterns described here are representative of global-scale phytoplankton dynamics.

## Conclusion

Based on our estimate, oceanic phytoplankton account for only  $\sim 0.06\%$  of the biomass of the biosphere (44)—a minuscule fraction despite their tremendous role in sustaining marine ecosystems and mediating Earth's carbon cycling. Accurate monitoring of this important group of organisms is necessary given current and projected increases in ocean temperatures (45), deoxygenation (46, 47), and acidification (48). This monitoring will require carbon-centric, depth-resolved measurements to account for subsurface phytoplankton as surface Chla does not account for subsurface patterns and is strongly affected by cell physiology (42).

We have shown here how global phytoplankton biomass and its spatiotemporal variability can be better understood from BGC-Argo observations of the subsurface ocean. Using this network of robotic profilers, we provided a first-order estimate for the global stock of phytoplankton carbon biomass as  $\sim 314 \text{ Tg}$ . The uncertainties associated with our estimate, not all of which are easily quantified, demonstrate the need for more direct observations of  $C_{\text{phy}}$  (49) and to better understand its relationship to  $b_{\text{bp}}$ .

We also highlight how the seasonal cycles of surface Chla do not provide an accurate picture of phytoplankton biomass for most of the ocean. This mismatch has implications for linking a Chla-based bloom phenology to the production and survival of higher trophic levels (e.g., zooplankton, larval fish), and for identifying a decoupling in predator–prey cycles due to climate change. Even though Chla is not a reliable proxy for determining biomass, it provides valuable information about the type and physiological state of phytoplankton present, especially when coupled with its long history of observation.

Since our analysis is based on climatological averages, real-time tracking of depth-resolved phytoplankton biomass on global scales will require more advanced methods—namely by combining the complementary observations from both satellite and float technologies. Satellites provide information across the ocean's surface, while floats provide information beneath it. By taking advantage of the synoptic global coverage of satellites combined with the vertical information from floats, gaps in float coverage could be filled using techniques like machine learning (50). Floats also collect data during times when observations from satellite ocean color cannot be made (e.g., at night, during polar winter, or under clouds). The combination of the two technologies will be an important step for the long-term monitoring of Earth's phytoplankton, and for understanding how they will be affected by anthropogenic climate change and potential geoengineering projects if implemented.

## Methods

**Bio-Optical Data from BGC-Argo Floats.** Water-column profiles of  $F_{\text{Chla}}$  and  $b_{\text{bp}}$  from BGC-Argo floats were obtained from multiple publicly available databases (51–55) and quality-controlled following established procedures [SI Appendix for more details, and SI Appendix, Table S1; (56–61)]. In brief, we checked  $F_{\text{Chla}}$  and  $b_{\text{bp}}$  profiles for unrealistic values, excessive measurement noise, inaccurate calibration offsets, and significant gaps in the vertical profiles. Parking hook effects on  $b_{\text{bp}}$  profiles were also removed. Profiles of  $F_{\text{Chla}}$  were corrected using a dark offset. The effects of nonphotochemical quenching in daytime profiles were corrected by

extrapolating the maximum mixed-layer value to the surface (52). The depth of the mixed layer was calculated by using a density threshold of  $0.03 \text{ kg m}^{-3}$  and a reference of 15 m (unless ice was potentially above; *SI Appendix*). Both bio-optical profiles were smoothed using median and mean filters. Alongside temperature and salinity, bio-optical data were binned and averaged to a 5-m resolution. Any missing data were interpolated with the smoothed, quality-controlled data points. If any near-surface data were missing, the shallowest mixed layer value was extrapolated upward. We only retained profiles where both  $F_{\text{Chla}}$  and  $b_{\text{bp}}$  data had passed quality control. We also visually inspected each float's history of profiles as a final step in quality control (*SI Appendix, Table S1*).

**Calculation of Carbon and Chla Climatology.** Using the weekly geometric mean profiles of  $F_{\text{Chla}}$  and  $b_{\text{bp}}$ ,  $\text{Chla}$  and  $C_{\text{phy}}$  were subsequently estimated from their bio-optical proxies as follows. To determine  $C_{\text{phy}}$ ,  $b_{\text{bp}}$  ( $\text{m}^{-1}$ ) was partitioned into phytoplankton ( $b_{\text{bp,phy}}$ ;  $\text{m}^{-1}$ ) and NAP ( $b_{\text{bp,NAP}}$ ;  $\text{m}^{-1}$ ) components, such that:

$$b_{\text{bp}} = b_{\text{bp,phy}} + b_{\text{bp,NAP}}$$

Often,  $C_{\text{phy}}$  is calculated by assuming a constant  $b_{\text{bp,NAP}}$  (e.g., refs. 18 and 19), however,  $b_{\text{bp,NAP}}$  likely varies with depth, season, and region (34). If  $b_{\text{bp,NAP}}$  variability is not considered, the conversion of  $b_{\text{bp}}$  to  $C_{\text{phy}}$  can lead to erroneous results (e.g., negative  $C_{\text{phy}}$  concentrations or overestimates of  $C_{\text{phy}}$  at depth).

To account for the spatiotemporal variability of  $b_{\text{bp,NAP}}$ , we calculated  $b_{\text{bp,NAP}}$  as a "background" value of  $b_{\text{bp}}$  for each weekly mean profile. Our approach aims to isolate the  $b_{\text{bp}}$  signal specific to phytoplankton, ensure that  $C_{\text{phy}}$  asymptotes to  $0 \text{ mg m}^{-3}$ , and eliminate any influence from intermediate particle layers. This approach builds on the offset correction from Arteaga et al. (23), who offset  $C_{\text{phy}}$  with reference values between 900 and 2,000 m depth. We calculated  $b_{\text{bp,NAP}}$  by utilizing all values of  $b_{\text{bp}}$  at depth (*SI Appendix, Fig. S3*). We first restricted measurements of  $b_{\text{bp}}$  to the deeper portion of the profile, where  $F_{\text{Chla}}$  concentrations are close to zero and  $b_{\text{bp}}$  is assumed to be dominated by NAP. To determine  $b_{\text{bp,NAP}}$ , we restricted the profile to  $b_{\text{bp}}$  values less than the profile's median  $b_{\text{bp}}$  and then applied a 1% quantile regression to the profile of this separated  $b_{\text{bp}}$ . Using this trend line, we defined a depth horizon equal to the shallowest depth where the  $b_{\text{bp}}$  profile intersects with the line. Below this depth horizon,  $b_{\text{bp,NAP}}$  is set equal to  $b_{\text{bp}}$ , where  $b_{\text{bp}}$  is expected to be largely NAP-dominated. Above this depth horizon,  $b_{\text{bp,NAP}}$  is set equal to  $b_{\text{bp}}$  at the point where the trend line intersects with the profile (i.e., the background value is extrapolated toward the surface). The resulting profile of  $b_{\text{bp,NAP}}$  is then used to estimate  $b_{\text{bp,phy}}$  by subtraction. This first approximation of  $b_{\text{bp,NAP}}$ , while imperfect, helps isolate the signal specific to phytoplankton (*SI Appendix, Comparison with Abundance-based Estimates*).

Phytoplankton  $C_{\text{phy}}$  (as  $\text{mg m}^{-3}$ ) is calculated as the product of  $b_{\text{bp,phy}}$  and a slope factor derived from direct estimates of  $C_{\text{phy}}$  correlated with  $b_{\text{bp}}$  at 470 nm (20, 49). Assuming a spectral slope of 0.73 to convert  $b_{\text{bp}}$  at 700 nm to  $b_{\text{bp}}$  at 470 nm (29):

$$C_{\text{phy}} = 12, 128 \times b_{\text{bp,phy}}$$

The slope factor from the work of Graff et al. (20) was based on  $b_{\text{bp}}$  (from both NAP and phytoplankton components). This differs from our approach, which partitions  $b_{\text{bp}}$  into NAP and phytoplankton components prior to applying the slope factor, which, alongside community-driven variability (33), could affect the statistical relationship between  $C_{\text{phy}}$  and  $b_{\text{bp}}$ . We assume that the  $C_{\text{phy}}:b_{\text{bp}}$  ratio is constant in our analysis.

Profiles of  $F_{\text{Chla}}$  based on the manufacturer's calibrations result in biases in the in situ determinations of Chla. We corrected for these biases using radiometric determinations of Chla similar to the procedure of Xing et al. (56) and Roesler et al. (58). This procedure involves using the diffuse attenuation coefficient ( $K_d$ ;  $\text{m}^{-1}$ ) of irradiance at 490 nm ( $E_{\text{d,490}}$ ;  $\text{W m}^{-2} \text{ nm}^{-1}$ ) to estimate Chla concentrations from an empirical relationship developed by Morel et al. (28). A slope factor, equal to the ratio of  $F_{\text{Chla}}$  and radiometric estimates of Chla, is then applied to correct for biases in  $F_{\text{Chla}}$ .

Before applying this correction, we quality-controlled  $E_{\text{d,490}}$  data similar to established procedures (62). First,  $E_{\text{d,490}}$  data outside of the range of  $-0.001$  and  $3.4 \text{ W m}^{-2} \text{ nm}^{-1}$  were discarded. If the profile still contained at least five data points, the sun's elevation was calculated. If the sun's elevation was less than  $2^\circ$ , the profile was not used because it was too dark to determine  $K_d$ . If the sun's elevation was greater than  $2^\circ$ , a dark value was determined and subtracted

from the irradiance profile following Organelli et al. (62). All irradiance values equal to or less than  $0 \text{ W m}^{-2} \text{ nm}^{-1}$  or from below this layer were labeled "bad"; otherwise, the remaining data were tentatively labeled "good." If more than five good data points were present, we fit a fourth-order polynomial to the irradiance profile of available good data points to identify variability from wave focusing and intermittent cloud cover. From this fit, data with residuals greater than two SD from the mean were labeled as bad. If this polynomial fit had an  $R^2$  greater than 0.995 and contained at least five good data points after this residual test, a second fourth-order polynomial fit was applied to identify weaker effects from wave focusing and clouds. The same procedure for identifying bad data was applied. If the fit of the second fourth-order polynomial fit was greater than 0.996, contained at least five good data points, and reached the 10 to 15 m depth bin, then a final fourth-order polynomial fit was applied and used to interpolate any missing values. From this quality-controlled profile,  $K_d$  within the 1% light level was calculated with a least-squares linear regression. The surface reference was estimated by extrapolating the polynomial fit to 0 m. Regressions with an  $R^2$  of less than 0.9, a  $K_d$  less than that of pure water ( $= 0.01660 \text{ m}^{-1}$ ) or greater than  $0.5 \text{ m}^{-1}$  [the limit suggested by Morel et al., (28)] were discarded. Using a similar procedure with the associated PAR data, we calculated  $K_d$  for PAR in the 1% light level (using only fits with a  $R^2 > 0.9$ ;  $n = 24,811$  profiles) and the first optical depth of PAR, equal to  $1/K_d$  of PAR. Then, Chla (in  $\text{mg m}^{-3}$ ) from  $K_d$  at 490 nm was calculated from the equation from Morel et al. (28):

$$\text{Chla} = \left( \frac{K_d - 0.01660}{0.077298} \right)^{1/0.67155}$$

Slope factors less than 0 and greater than 30 were discarded. From the original 39,982 profiles of  $E_{\text{d,490}}$ , a total of 23,694 slope factors were obtained (*SI Appendix, Fig. S2*). The arithmetic mean of all these slope factors equals  $\sim 1.8$ , which is lower but close to Roesler et al.'s mean value using a smaller sample size of float profiles (58). Slope factors in the Southern Ocean also have similar values to those by Schallenberg et al. (63). Since individual calibrations for each profile are not possible (not all BGC-Argo floats have both radiometers and fluorometers), we instead calculated the annual geometric mean slope factor from all available monthly geometric means for each region in the analysis. In other words, a single regional slope factor was applied to the weekly climatologies of  $F_{\text{Chla}}$  to achieve more accurate estimates of Chla.

Overall, this process yielded weekly depth profiles Chla and  $C_{\text{phy}}$  for every  $10^\circ$  latitude band for the Atlantic, Pacific, and Indian Ocean basins. This weekly climatology and the associated mixed-layer depth were then concatenated three times, interpolated for any data that were missing, and then smoothed along the temporal axis with a nine-point rolling median followed by a nine-point rolling mean. The center of the smoothed series is used in this analysis. If data were missing in a latitudinal band, data from the nearest region were extrapolated (these extrapolated data represent  $< 1\%$  of the ocean's surface area and include  $60\text{--}70^\circ\text{N}$  in the Pacific Ocean,  $80\text{--}90^\circ\text{N}$  in the Atlantic Ocean, and  $70\text{--}80^\circ\text{S}$  in the Indian Ocean; *SI Appendix, Fig. S1*). From these regions, we calculated the global-scale seasonal cycle for every  $10^\circ$  latitude band as the weekly, geometric mean weighted by surface area. The annual stocks (as represented in Fig. 2) are calculated as the geometric mean of the global-scale seasonal cycles. The geometric mean was used because it estimates the median value when the data is log-normally distributed. We also wanted to avoid noise associated with outliers, especially in data-poor regions (stocks based on the arithmetic mean are reported in *SI Appendix*).

**Uncertainty in Carbon and Chla.** We quantified the error in both our  $C_{\text{phy}}$  and Chla estimates from floats. For this, we considered only the uncertainty in the conversion of the bio-optical parameter to biological mass and assumed that errors due to sensor drift, temperature, biofouling, and model sensor calibrations are negligible. We calculated the MAPE as:

$$\text{MAPE} = \frac{1}{N} \sum_{i=0}^{N-1} \frac{|y_i - \hat{y}_i|}{|y_i|} \times 100\%$$

where  $y_i$  is the actual value of  $C_{\text{phy}}$  or Chla, and  $\hat{y}_i$  is the predicted value of  $C_{\text{phy}}$  or Chla. The uncertainty in converting  $b_{\text{bp}}$  to  $C_{\text{phy}}$  was determined from a linear least-squares regression applied to the data digitized from Graff et al.'s Fig. 2

(20). We found the same slope and y-intercept of the regression reported by the authors. We used this equation to calculate a MAPE of ~32% for  $C_{\text{phy}}$ . The MAPE for Chla depends on the region (SI Appendix, Fig. S2) but the final error in the global stock of Chla comes to ~31%.

**Satellite Chla Climatology.** To compare with float observations of surface Chla and  $\Sigma C_{\text{phy}}$ , we created weekly climatologies of satellite-based surface Chla using level-3 data from the Moderate Resolution Imaging Spectrometer (MODIS) Aqua satellite. We obtained 8-d surface Chla data with a 9-km spatial resolution for the period of January 1, 2012, to December 31, 2023. This date range approximately covers the period when most of the float data was collected. All satellite values were used in the calculation of Chla climatologies (as opposed to matching up satellite measurements with profiles). For each 8-d image, we calculated the average Chla concentration for every 10° latitude and only retained averages that had more than 70% of pixels available. These averages were used to calculate a mean weekly climatology for each latitude band and to compare with float observations. Similar to the float climatology, satellite Chla was concatenated three times and smoothed with a three-point rolling median followed by a three-point rolling mean, using the center 52 wk of data for analysis.

**Bloom Metrics.** We characterized the annual cycle of phytoplankton with three phenological metrics: 1) the timing of the bloom peak, 2) the blooming period, and 3) the bloom amplitude. These metrics were calculated using  $\Sigma C_{\text{phy}}$  and surface Chla. Prior to calculating these metrics, the global-scale, weekly time-series of  $\Sigma C_{\text{phy}}$  and surface Chla were smoothed with a six-point rolling median, followed by a six-point rolling mean. This additional smoothing was performed to limit noise associated with averaging the basin-specific climatologies and for calculating the accumulation rate. The timing of the peak bloom is defined as the week when  $\Sigma C_{\text{phy}}$  or surface Chla reaches its annual maximum. The blooming period was defined as the total number of weeks where the accumulation rate of  $\Sigma C_{\text{phy}}$  or surface Chla is greater than  $0 \text{ d}^{-1}$  [based on Behrenfeld and Boss's definition of "blooming," (42)]. To limit outliers, we applied a three-point rolling mean to smooth the latitudinal variation in the blooming period. To give a sense of the relative variation in each region's seasonal cycle, the bloom amplitude was defined as the maximum in  $\Sigma C_{\text{phy}}$  or Chla minus the minimum and divided by

the annual mean (43). The same metrics were also calculated for satellite Chla to compare with surface Chla detected by floats. Pearson correlation coefficients were determined using surface Chla vs.  $\Sigma C_{\text{phy}}$  and surface Chla vs. satellite Chla (SI Appendix, Fig. S6), all of which were log-transformed prior to determining the correlation coefficient. For satellite observations, the correlation coefficient, bloom amplitude, and bloom duration were only calculated when satellite data was available for at least 47 wk of the year. Additional metrics describing the seasonal cycle, such as the timing of the minimum accumulation rate, are also reported in SI Appendix, Fig. S7.

**Data, Materials, and Software Availability.** All code and processed data from this analysis are available on Zenodo (DOI: [10.5281/zenodo.10949682](https://doi.org/10.5281/zenodo.10949682)) (64). Previously published data were used for this work. All data used in the article are publicly available and referred to in the *Methods* and SI Appendix (51–55, 65).

**ACKNOWLEDGMENTS.** Portions of the paper were developed from the thesis of A.C.S. We thank Dr. John Cullen, Dr. Emmanuel Boss, Dr. Andrew Irwin, Dr. Blair Greenan, and Jessica Oberlander for providing helpful feedback during the development of this manuscript. We acknowledge support to A.C.S. by a Nova Scotia Graduate Student scholarship, a Canada Graduate Scholarship (Master's) from the Natural Sciences and Engineering Research Council of Canada (NSERC), an NSERC Discovery Grant (RGPIN-2014-03938), and the Ocean Frontier Institute (Phase-2-NWA-BCP). We thank the NASA Ocean Biology Distributed Active Archive Center (<https://oceancolor.gsfc.nasa.gov/>) for processing and making available the MODIS-Aqua satellite imagery used in this analysis. We thank all those involved in the deployment and processing of the BGC-Argo float observations. BGC-Argo float data were made publicly available by the International Argo Program and the national programs that contribute to it (<https://argo.ucsd.edu> and <https://www.ocean-ops.org>). The Argo Program is part of the Global Ocean Observing System. Additional BGC-Argo float data were also made publicly available by the Gulf of Mexico Research Initiative Information and Data Cooperative at <https://data.gulfresearchinitiative.org>, the National Oceanographic and Atmospheric Association's National Centers for Environmental Information, and the North Atlantic Aerosol and Marine Ecosystem Study campaign (<https://misclab.ume-maine.edu/floats/>).

1. C. B. Field, M. J. Behrenfeld, J. T. Randerson, P. Falkowski, Primary production of the biosphere: Integrating terrestrial and oceanic components. *Science* **281**, 237–240 (1998).
2. P. Parekh, S. Dutkiewicz, M. J. Follows, T. Ito, Atmospheric carbon dioxide in a less dusty world. *Geophys. Res. Lett.* **33**, L03610 (2006).
3. H. R. Gordon *et al.*, Phytoplankton pigment concentrations in the Middle Atlantic Bight: Comparison of ship determinations and CZCS estimates. *Appl. Optics* **22**, 20 (1983).
4. J. A. Yoder, C. R. McClain, G. C. Feldman, W. E. Esaias, Annual cycles of phytoplankton chlorophyll concentrations in the global ocean: A satellite view. *Global Biogeochem. Cycles* **7**, 181–193 (1993).
5. D. A. Siegel, S. C. Doney, J. A. Yoder, The north atlantic spring phytoplankton bloom and sverdrup's critical depth hypothesis. *Science* **296**, 730–733 (2002).
6. J. A. Yoder, M. A. Kennelly, Seasonal and ENSO variability in global ocean phytoplankton chlorophyll derived from 4 years of SeaWiFS measurements. *Global Biogeochem. Cycles* **17**, 1112 (2003).
7. T. Platt, S. Sathyendranath, Ecological indicators for the pelagic zone of the ocean from remote sensing. *Remote Sens. Environ.* **112**, 3426–3436 (2008).
8. S. A. Henson, H. S. Cole, J. Hopkins, A. P. Martin, A. Yool, Detection of climate change-driven trends in phytoplankton phenology. *Global Change Biol.* **24**, e101–e111 (2018).
9. S. J. Thomalla, S.-A. Nicholson, T. J. Ryan-Keogh, M. E. Smith, Widespread changes in southern ocean phytoplankton blooms linked to climate drivers. *Nat. Clim. Change* **13**, 975–984 (2023).
10. H. R. Gordon, W. R. McCluney, Estimation of the depth of sunlight penetration in the sea for remote sensing. *Appl. Optics* **14**, 413 (1975).
11. J. J. Cullen, The deep chlorophyll maximum: Comparing vertical profiles of chlorophyll a. *Can. J. Fisher. Aquat. Sci.* **39**, 791–803 (1982).
12. P. G. Falkowski, The role of phytoplankton photosynthesis in global biogeochemical cycles. *Photosynth. Res.* **39**, 235–258 (1994).
13. R. J. Geider, H. L. MacIntyre, T. M. Kana, A dynamic regulatory model of phytoplankton acclimation to light, nutrients, and temperature. *Limnol. Oceanogr.* **43**, 679–694 (1998).
14. J. H. Steele, A study of production in the gulf of mexico. *J. Marine Res.* **22**, 211–222 (1964).
15. J. J. Cullen, Subsurface chlorophyll maximum layers: Enduring enigma or mystery solved? *Annu. Rev. Marine Sci.* **7**, 207–239 (2015).
16. K. Fennel, E. Boss, Subsurface maxima of phytoplankton and chlorophyll: Steady-state solutions from a simple model. *Limnol. Oceanogr.* **48**, 1521–1534 (2003).
17. Y. Masuda *et al.*, Photoacclimation by phytoplankton determines the distribution of global subsurface chlorophyll maxima in the ocean. *Commun. Earth Environ.* **2**, 128 (2021).
18. M. J. Behrenfeld, E. Boss, D. A. Siegel, D. M. Shea, Carbon-based ocean productivity and phytoplankton physiology from space. *Global Biogeochem. Cycles* **19**, GB1006 (2005).
19. V. Martinez-Vicente, G. Dall'Olmo, G. Tarran, E. Boss, S. Sathyendranath, Optical backscattering is correlated with phytoplankton carbon across the atlantic ocean. *Geophys. Res. Lett.* **40**, 1154–1158 (2013).
20. J. R. Graff *et al.*, Analytical phytoplankton carbon measurements spanning diverse ecosystems. *Deep Sea Res. Part I.* **102**, 16–25 (2015).
21. E. Boss, M. Behrenfeld, In situ evaluation of the initiation of the North Atlantic phytoplankton bloom. *Geophys. Res. Lett.* **37**, L18603 (2010).
22. T. K. Westberry *et al.*, Annual cycles of phytoplankton biomass in the subarctic atlantic and pacific ocean. *Global Biogeochem. Cycles* **30**, 175–190 (2016).
23. L. A. Arteaga, E. Boss, M. J. Behrenfeld, T. K. Westberry, J. L. Sarmiento, Seasonal modulation of phytoplankton biomass in the southern ocean. *Nat. Commun.* **11**, 5364 (2020).
24. B. Yang *et al.*, Phytoplankton Phenology in the north atlantic: Insights from profiling float measurements. *Front. Marine Sci.* **7**, 139 (2020).
25. S. M. Chiswell *et al.*, Seasonal cycles of phytoplankton and net primary production from biogeochemical argo float data in the south-west pacific ocean. *Deep Sea Res. Part I* **187**, 103834 (2022).
26. C. R. Vives, C. Schallenberg, P. G. Strutton, P. W. Boyd, Biogeochemical-Argo floats show that chlorophyll increases before carbon in the high-latitude Southern ocean spring bloom. *Limnol. Oceanogr. Lett.* **9**, 172–182 (2023), [10.1002/lol2.10322](https://doi.org/10.1002/lol2.10322).
27. A. C. Stoer *et al.*, A census of quality-controlled biogeochemical-argo float measurements. *Front. Marine Sci.* **10**, 1233289 (2023).
28. A. Morel *et al.*, Examining the consistency of products derived from various ocean color sensors in open ocean (Case 1) waters in the perspective of a multi-sensor approach. *Remote Sens. Environ.* **111**, 69–88 (2007).
29. E. Boss *et al.*, The characteristics of particulate absorption, scattering and attenuation coefficients in the surface ocean; Contribution of the tara oceans expedition. *Methods Oceanogr.* **7**, 52–62 (2013).
30. R. D. Vaillancourt, Light backscattering properties of marine phytoplankton: Relationships to cell size, chemical composition and taxonomy. *J. Plankton Res.* **26**, 191–212 (2004).
31. G. Neukermans, H. Loisel, X. Mériaux, R. Astoreca, D. McKee, In situ variability of mass-specific beam attenuation and backscattering of marine particles with respect to particle size, density, and composition. *Limnol. Oceanogr.* **57**, 124–144 (2012).
32. C. Poulin, D. Antoine, Y. Huot, Diurnal variations of the optical properties of phytoplankton in a laboratory experiment and their implication for using inherent optical properties to measure biomass. *Opt. Express* **26**, 711 (2018).
33. J. Fox *et al.*, An absorption-based approach to improved estimates of phytoplankton biomass and net primary production. *Limnol. Oceanogr.* **7**, 419–426 (2022).
34. M. Bellacicco *et al.*, Global variability of optical backscattering by non-algal particles from a biogeochemical-argo data set. *Geophys. Res. Lett.* **46**, 9767–9776 (2019).
35. N. Baetge *et al.*, Physiological and interspecific factors determine diel changes in phytoplankton bio-optical properties. *Limnol. Oceanogr.* **69**, 390–407 (2024).

36. H. R. Gordon, A. Morel, *Remote Assessment of Ocean Color for Interpretation of Satellite Visible Imagery: A Review* (Springer-Verlag, 1983).
37. P. Falkowski, J. Raven, "Aquatic photosynthesis in biogeochemical cycles" in *Aquatic Photosynthesis* (Princeton University Press, 1997), p. 389.
38. E. T. Buitenhuis *et al.*, MAREDAT: Towards a world atlas of MARine Ecosystem DATA. *Earth Syst. Sci. Data* **5**, 227–239 (2013).
39. D. Antoine, J. André, A. Morel, Oceanic primary production: 2. Estimation at global scale from satellite (Coastal Zone Color Scanner) chlorophyll. *Global Biogeochem. Cycles* **10**, 57–69 (1996).
40. M. J. Behrenfeld, P. G. Falkowski, Photosynthetic rates derived from satellite-based chlorophyll concentration. *Limnol. Oceanogr.* **42**, 1–20 (1997).
41. Y. M. Bar-On, R. Milo, The biomass composition of the oceans: A blueprint of our blue planet. *Cell* **179**, 1451–1454 (2019).
42. M. J. Behrenfeld, E. S. Boss, Student's tutorial on bloom hypotheses in the context of phytoplankton annual cycles. *Global Change Biol.* **24**, 55–77 (2018).
43. J. E. Cloern, A. D. Jassby, Complex seasonal patterns of primary producers at the land-sea interface. *Ecol. Lett.* **11**, 1294–1303 (2008).
44. Y. M. Bar-On, R. Phillips, R. Milo, The biomass distribution on Earth. *Proc. Natl. Acad. Sci. U.S.A.* **115**, 6506–6511 (2018).
45. L. Cheng *et al.*, Past and future ocean warming. *Nat. Rev. Earth Environ.* **3**, 776–794 (2022).
46. S. Schmidtko, L. Stramma, M. Visbeck, Decline in global oceanic oxygen content during the past five decades. *Nature* **542**, 335–339 (2017).
47. D. Breitburg *et al.*, Declining oxygen in the global ocean and coastal waters. *Science* **359**, eaam7240 (2018).
48. S. C. Doney, V. J. Fabry, R. A. Feely, J. A. Kleypas, Ocean acidification: The other CO<sub>2</sub> problem. *Annu. Rev. Marine Sci.* **1**, 169–192 (2009).
49. J. R. Graff, A. J. Milligan, M. J. Behrenfeld, The measurement of phytoplankton biomass using flow-cytometric sorting and elemental analysis of carbon. *Limnol. Oceanogr. Methods* **10**, 910–920 (2012).
50. R. Sauzède *et al.*, A neural network-based method for merging ocean color and argo data to extend surface bio-optical properties to depth: Retrieval of the particulate backscattering coefficient. *J. Geophys. Res. Oceans* **121**, 2552–2571 (2016).
51. P. Hamilton, Leidos, Data from "Ocean currents, temperatures, and others measured by drifters and profiling floats for the Lagrangian approach to Study the Gulf of Mexico deep circulation project 2011-07 to 2015-06 (NCEI Accession 0159562)". NOAA National Centers for Environmental Information. <https://data.nodc.noaa.gov/cgi-bin/iso?id=gov.noaa.nodc:159562>. Deposited 24 October 2017.
52. L. Shay *et al.*, Data from "Conductivity, temperature, and depth (CTD) data collected from R/V F.G. Walton Smith cruise WS17121 in the northeastern Gulf of Mexico from 2017-05-02 to 2017-05-07". *Gulf of Mexico Research Initiative Information and Data Cooperative (GRIIDC)*, <https://doi.org/10.7266/N7NZ8682>. Deposited 3 October 2018.
53. M. J. Behrenfeld *et al.*, The north atlantic aerosol and marine ecosystem study (NAAMES): Science motive and mission overview. *Front. Marine Sci.* **6**, 122 (2019).
54. C. Gordon, K. Fennel, C. Richards, L. Shay, J. Brewster, Can ocean community production and respiration be determined by measuring high-frequency oxygen profiles from autonomous floats? *Biogeosciences* **17**, 4119–4134 (2020).
55. Argo, Data from "Argo float data and metadata from global data assembly centre (Argo GDAC)". SEANOE. <https://doi.org/10.17882/42182>. Accessed 3 February 2024.
56. X. Xing *et al.*, Combined processing and mutual interpretation of radiometry and fluorimetry from autonomous profiling bio-argo floats: Chlorophyll a retrieval. *J. Geophys. Res.* **116**, C06020 (2011).
57. X. Xing *et al.*, Quenching correction for in vivo chlorophyll fluorescence acquired by autonomous platforms: A case study with instrumented elephant seals in the Kerguelen region (Southern Ocean). *Limnol. Oceanogr. Methods* **10**, 483–495 (2012).
58. C. Roesler *et al.*, Recommendations for obtaining unbiased chlorophyll estimates from in situ chlorophyll fluorometers: A global analysis of WET Labs ECO sensors. *Limnol. Oceanogr. Methods* **15**, 572–585 (2017).
59. G. Dall'Olmo *et al.*, Real-time quality control of optical backscattering data from biogeochemical-Argo floats. *Open Res. Eur.* **2**, 118 (2023).
60. G. Dall'Olmo *et al.*, BGC Argo Quality Control Manual for Particles Backscattering, Version 1.0 (Ifremer, Brest, France, 2023).
61. C. Schmechtig *et al.*, BGC-Argo Quality Control Manual for the Chlorophyll-a Concentration, Version 3.0 (Ifremer, Brest, France, 2023).
62. E. Organelli *et al.*, A novel near-real-time quality-control procedure for radiometric profiles measured by bio-argo floats: Protocols and performances. *J. Atmos. Oceanic Technol.* **33**, 937–951 (2016).
63. C. Schallenberg, R. F. Strzepek, S. Bestley, B. Wojtasiewicz, T. W. Trull, Iron limitation drives the globally extreme fluorescence/chlorophyll ratios of the southern ocean. *Geophys. Res. Lett.* **49**, e2021GL097616 (2022).
64. A. Stoer, K. Fennel, Data from "Data and processing from "Carbon-centric dynamics of Earth's marine phytoplankton". Zenodo. <https://doi.org/10.5281/zenodo.10949682>. Deposited 1 October 2024.
65. E. T. Buitenhuis *et al.*, Picophytoplankton biomass distribution in the global ocean. *Earth Syst. Sci. Data* **4**, 37–46 (2012).